JACS Au
AN OPEN ACCESS JOURNAL OF THE AMERICAN CHEMICAL SOCIETY

pubs.acs.org/jacsau
Article

Distorted Surface Ensembles in Platinum−Antimony for the Durable Catalytic Dehydrogenation of Methylcyclohexane

Yuki Nakaya,* Aoto Okada, and Shinya Furukawa*

Cite This: JACS Au 2025, 5, 1956−1964
Read Online

ACCESS | Metrics & More | Article Recommendations | Supporting Information

ABSTRACT: Geometric and electronic effects are particularly pronounced when catalyzing small molecules, which require small active-metal ensembles. Researchers have been intensively focused on the alloy catalysis of small molecules. However, when large molecules are catalyzed, large active-metal ensembles are preferable to small active-metal ensembles. The catalysis with large ensembles in alloys proceeds more efficiently than that with pure metals because of the geometric and electronic effects of diluent metals. However, it is difficult to significantly improve the catalytic performance because of the limited changes in the geometric and electronic features in active-metal-rich compositions. Thus, we employed distorted active-metal ensembles, which are expected to have unique adsorptivity/reactivity for large molecules. We found that the unique crystal structure of Pt_3Sb showed distorted Pt_3 ensembles shaped as isosceles triangles, which differ from the standard Pt_3 ensembles shaped as regular triangles. We used methylcyclohexane dehydrogenation as a proof-of-concept reaction, which shows that the feature of Pt_3 ensembles is crucial for catalytic performance. Theoretical and experimental results revealed that the distorted Pt_3@Pt_3Sb catalyst effectively suppressed the side reactions and exhibited considerably higher durability than the standard Pt_3 ensembles, represented by the Pt_3@Pt_3Sn catalyst, highlighting the importance of the Pt_3 shape.

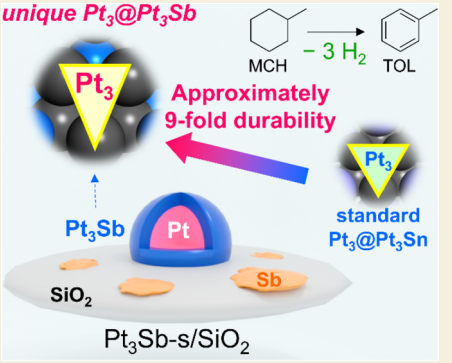

KEYWORDS: *alloy, geometric effect, ensembles, distortion, hydrogen production*

INTRODUCTION

Alloy materials have been used as useful platforms for improving catalytic performance by changing their compositions and structures.[1−3] Since the advent of alloy catalysis, geometric (ensemble) and electronic effects have played important roles. These effects are particularly pronounced in small molecule catalysis, which requires small active-metal ensembles.[4−14] The ensembles are obtained by alloying the active metal with equal or excess amounts of diluent metals. Resultantly, both geometric and electronic properties are dramatically altered compared with those of the parent monometallic systems. One of the recent trends in alloy catalysis is the complete isolation of active metals with maximized ensemble effects. However, it is highly important to use large active-metal ensembles (A_n, n is the number of atoms forming the ensembles, $n \geq 3$) when catalyzing large molecules (such as methylcyclohexane (MCH) dehydrogenation,[15,16] toluene hydrogenation,[17] and Suzuki−Miyaura cross-coupling).[18] A_n ensembles are obtained using an A-rich alloy; therefore, the electronic modification by B (B: second metals) is small. Additionally, to maximize the exposure of A_n ensembles, the well-designed reaction environments of intermetallic compounds are preferable to random surface atomic arrangements (*e.g.*, a mixture of A_n (n = 1−4)) of solid-solution alloys.[1,4,15,17,19,20] Regarding A_3 catalysis, the conventional crystal structures of Cu_3Au-type (*fcc*) intermetallic compounds have A_3 ensembles (equilateral triangles), which are effective for various reactions,[1−3] on the most stable (111) facet. The A_3 ensembles expand/shrink in an equirectangular manner, depending on the atomic radius of the second metal. Therefore, it is difficult to dramatically change the geometric properties of the A_3 ensembles. The A_3 ensembles in Cu_3Au-type alloys facilitate efficient catalysis of large molecules. However, it is difficult to dramatically improve the catalytic performance using conventional A_3 ensembles. Thus, this problem needs to be solved under structural constraints when necessary to achieve a drastic improvement in catalysis for large molecules.

A possible approach to addressing this issue is the use of distorted A_3 ensembles. If the shapes of A_3 ensembles are highly distorted (inequivalent bond distances and angles of the ensembles), the adsorptivity/reactivity of large molecules would be greatly altered, resulting in a unique catalytic performance. However, it is considerably difficult to obtain such distorted ensembles because of the predominance of

Received: February 18, 2025
Revised: March 12, 2025
Accepted: March 12, 2025
Published: March 19, 2025

https://doi.org/10.1021/jacsau.5c00181
JACS Au 2025, 5, 1956−1964

Scheme 1. (a) Elements That Can Form Pt_3M (Cu_3Au-type) with Pt Are Highlighted by Magenta in the Periodic Table. (b) Unit Cell, Wulff Construction, and the Most Stable Surface Plane of the Pt_3Sb. The Wulff Construction Is Drawn Using the VESTA Software.[21] (c) Unit Cell and the Most Stable Surface of the Pt_3Sn. The Surfaces of (b) Pt_3Sb and (c) Pt_3Sn Are Optimized Using the Cambridge Sequential Total Energy Package Code.[22] (d) Illustration of the Entangled Geometric−Electronic Relationship in Alloy Catalysis

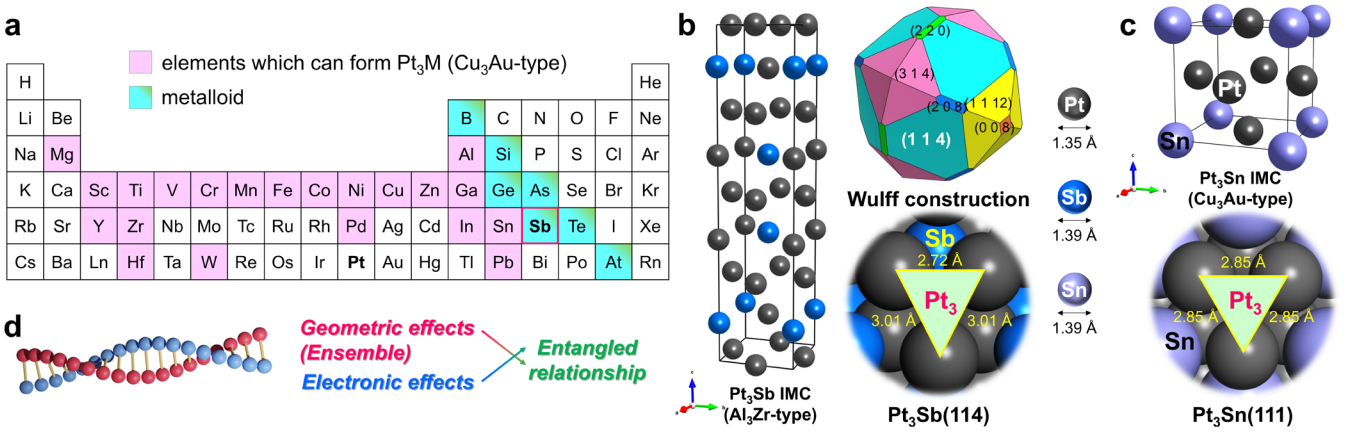

ordered Cu_3Au-type structures or random solid-solution alloys (Scheme 1a).[1−3] In this context, we focus on intermetallic compounds containing a metalloid as a component. The incorporation of a metalloid affords a crystal structure considerably different from the incorporation of a transition metal, even if the ratio to the active metal is identical.[1−3] We have investigated a database of various active metal−metalloid alloys and found that Pt_3Sb (Al_3Zr-type) displays distorted Pt_3 ensembles on the surface (AtomWork database of the National Institute for Materials Science (http://crystdb.nims.go.jp/)). The calculation of surface energies for various facets by density functional theory (DFT) calculations confirms that Pt_3Sb exposes the Pt_3 ensemble on the most stable (114) facet (Scheme 1b).

Guided by this finding, we synthesized Pt_3Sb and evaluated its catalytic performance for MCH dehydrogenation as a proof-of-concept reaction. Liquid organic hydrogen carriers have been considered attractive alternatives for hydrogen storage. Among them, the reversible toluene−MCH system is the most promising one because of its high hydrogen content, low toxicity, and availability in the existing petroleum infrastructure.[23−25] However, MCH dehydrogenation, which is the hydrogen release process of this system, is a challenging reaction. Conventional catalysts are readily deactivated in a short time because of coke formation; therefore, the main challenge is to develop durable catalysts.[1,15,16,25,26] In this reaction, the equirectangular Pt_3 ensembles in Pt_3M (Cu_3Au-type) have been reported to improve the catalytic durability compared to monometallic Pt. However, their durability is insufficient and requires improvement.[1,2,15] In this context, we synthesize two types of intermetallic compounds and demonstrate the importance of the Pt_3 shape. Two different shapes of the Pt_3 ensembles are provided by the (111) surface of Cu_3Au-type Pt_3Sn and the (114) surface of $ZrAl_3$-type Pt_3Sb, respectively. The former is an equirectangular triangle, whereas the latter is an isosceles triangle (Scheme 1b,c). The distorted Pt_3@Pt_3Sb(114) effectively suppresses the side reactions (eventual coke formation), thereby exhibiting considerably higher durability than the equirectangular Pt_3@Pt_3Sn(111), highlighting the importance of the Pt_3 shape. Interestingly, Pt_3Sb(114) and Pt_3Sn(111) have similar electronic structures probably because Sb is next to Sn in the periodic table and the atomic radius of Sb (1.39 Å) is almost the same as that of Sn (1.39 Å) (Figure S1).[27] Therefore, only the ensemble shapes are different for Pt_3Sb and Pt_3Sn. Interestingly, using these Pt_3 ensembles, we have succeeded in decoupling geometric effects from the entangled geometric−electronic relationship in alloy catalysis for the first time (Scheme 1d). It has long been a great challenge to separate the geometric and electronic effects in catalysis from those that correlate with each other. Although the separation of electronic effects is not difficult, there have been no reports on the separation of geometric effects because of its difficulty (the hurdle of separating geometric effects in alloy catalysis is described in Supporting Note 1). This work provides a dimension for the design of high-performance catalysts for broad applications and for an in-depth understanding of catalysis.

Here, we have demonstrated the importance of the Pt_3 shape. Two different shapes of the Pt_3 ensembles are provided by Cu_3Au-type Pt_3Sn and $ZrAl_3$-type Pt_3Sb, respectively. The former is an equirectangular triangle, whereas the latter is an isosceles triangle. These alloy materials have similar electronic structures, and the atomic radii are almost the same. Therefore, only the Pt_3 shapes are significantly different between these alloy materials. Interestingly, Pt_3Sb exhibits a considerably higher durability than Pt_3Sn for the test reaction of MCH dehydrogenation. Theoretical and experimental results show that the distorted Pt_3 ensembles of Pt_3Sb effectively suppress the side reactions and exhibit considerably higher catalyst durability than the normal Pt_3 ensembles of Pt_3Sn. This study not only shows the impact of the ensemble shape but also demonstrates the decoupling of the geometric effect of alloy catalysis from the entanglement geometric−electronic relationship for the first time. This work provides an effective strategy for exploring fundamental insights into alloy catalysis, and thus, it helps to design catalysts with unprecedented properties.

RESULTS AND DISCUSSION

Theoretical Prediction for Selectivity/Durability

First, we used DFT calculations to predict the most stable facets of the Pt_3 ensembles and the durability of the catalysts.

https://doi.org/10.1021/jacsau.5c00181
JACS Au 2025, 5, 1956−1964

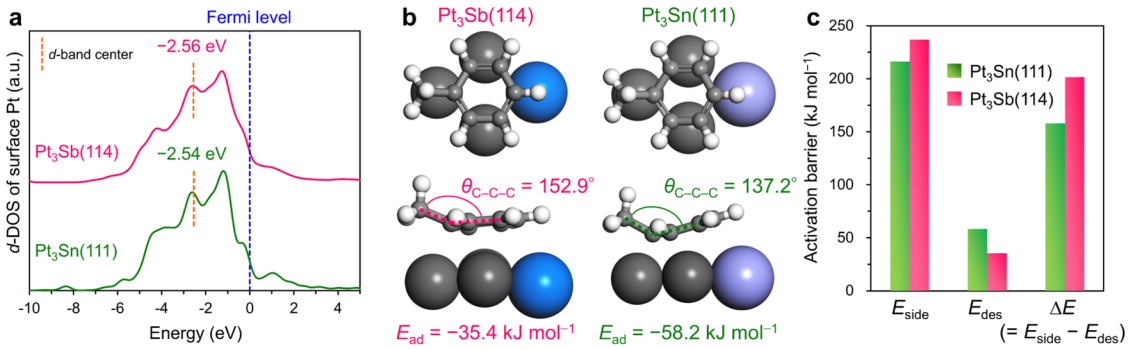

Figure 1. (a) Density of states of $Pt_3Sn(111)$ and $Pt_3Sb(114)$ projected on the d orbitals of surface Pt atoms. (b) Adsorption configuration of toluene on the $Pt_3Sb(114)$ and $Pt_3Sn(111)$ surfaces. (c) Energy barriers of the demethylation of toluene (E_{side}), desorption of toluene (TOL) (E_{des}), and difference between E_{side} and E_{des} ($\Delta E = E_{side} - E_{des}$) on $Pt_3Sn(111)$ and $Pt_3Sb(114)$.

In our models, the (114) and (111) planes were used for Pt_3Sb and Pt_3Sn, respectively. For Pt_3Sb, we calculated the surface energies for various facets and illustrated the Wulff constructions (Figures S2 and S3).

The equilibrium crystal shape of Pt_3Sb determined by Wulff constructions primarily comprises the (114), (1112), and (314) planes. Interestingly, given the crystallographically unique crystal structure, distorted Pt_3 ensembles were observed in these planes. The (114) plane is the most stable facet of the Pt_3Sb crystal and is dominant for the nanoparticles. Therefore, $Pt_3Sb(114)$ was used in this study. For Pt_3Sn, we chose the (111) plane, which is the most stable surface for the Pt_3M (Cu_3Au-type).[1,28−30] The optimized surface atomic arrangements of $Pt_3Sb(114)$ and $Pt_3Sn(111)$ are shown in Scheme 1b,c, respectively. The shape of the Pt_3 ensembles on $Pt_3Sn(111)$ is an equilateral triangle with an atomic distance of 2.85 Å. In contrast, the Pt_3 on $Pt_3Sb(114)$ comprises an isosceles triangle (equal: 3.01 Å, base: 2.72 Å). Figure 1 shows the density of states and the corresponding d-band center (ε_d) projected on the d orbitals. No significant difference in the d-band shapes and centers was observed between $Pt_3Sb(114)$ and $Pt_3Sn(111)$. Therefore, this comparison can exclude the electronic effect, allowing us to focus on the importance of the Pt_3 shape. Alternatively, the difference between the $Pt_3Sb(114)$ and $Pt_3Sn(111)$ surfaces is only the geometric environment of Pt_3, that is, whether the Pt_3 sites are distorted or not.

Using the modeled surfaces, we theoretically predicted the catalyst's durability. The trend in selectivity/durability for dehydrogenation reactions has typically been rationalized using the difference between the energy barriers of product desorption (main pathway) and decomposition (side pathway).[4,5,7,9,31,32] Therefore, we calculated the difference in the energy barriers ($\Delta E = E_{side} - E_{des}$) between toluene desorption (E_{des}) and toluene demethylation (E_{side}: $C_6H_5CH_3 \rightarrow C_6H_5 + CH_3$). For MCH dehydrogenation, the toluene demethylation is the rate-determining step of the side reactions, eventually accumulating coke.[15,25,33] Therefore, whether the as-generated toluene desorbs from the surface or the reaction proceeds further determines the rate of coke formation (durability). Figure 1b shows the adsorption configurations of toluene on $Pt_3@Pt_3Sb(114)$ and $Pt_3@Pt_3Sn(111)$. It is clear that the angle of the methyl group relative to the benzene ring is obviously different, confirming the influence of the Pt_3 shape. Figure 1c summarizes the energy barriers of E_{side}, E_{des}, and ΔE calculated for $Pt_3@Pt_3Sn(111)$ and $Pt_3@Pt_3Sb(114)$ (see Figure S4 for the detailed structures). $Pt_3@Pt_3Sb(114)$ showed a higher E_{side} value of 236.9 kJ mol^{-1} than $Pt_3@Pt_3Sn(111)$ (216.2 kJ mol^{-1}), whereas it showed a lower E_{des} value of 35.4 kJ mol^{-1} than $Pt_3@Pt_3Sn(111)$ (58.2 kJ mol^{-1}). These results indicated that $Pt_3@Pt_3Sb(114)$ could effectively suppress the demethylation while promoting the desorption of toluene probably due to the distortion of Pt_3. Therefore, $Pt_3@Pt_3Sb(114)$ had a considerably higher ΔE value of 201.4 kJ mol^{-1} than $Pt_3@Pt_3Sn(111)$ (158.0 kJ mol^{-1}). As stated, the difference between these surfaces is only the geometric environment, that is, whether the Pt_3 ensembles are distorted or not. Hence, these results suggested the high catalytic durability of the distorted Pt_3 ensembles in Pt_3Sb for MCH dehydrogenation.

Structural Analysis of Silica-Supported Platinum−Antimony Catalysts

To demonstrate the transferability from theoretical hypothesis to practical catalytic reaction, we synthesized Pt−Sb alloy catalysts supported on SiO_2 with different Pt/Sb atomic ratios by the pore-filling co-impregnation method.[4−7,15,36] The catalysts with Pt/Sb ratios of 1.5 and 2.7 were designated as Pt_3Sb/SiO_2 and Pt_3Sb-s/SiO_2, respectively. Figure S5 shows the H_2 temperature-programmed reduction (H_2-TPR) profile of the as-prepared (nonreduced) catalyst. The hydrogen consumption was completed by 700 °C. Unless otherwise stated, the as-prepared catalysts were reduced at 700 °C for 1 h before the characterization and catalytic reactions. Figure 2 shows the X-ray diffraction (XRD) patterns. The diffraction patterns of the Pt_3Sb/SiO_2 catalyst significantly corresponded with that of the referential Pt_3Sb (Zr_3Al-type), indicating the formation of Pt_3Sb nanoparticles. The small broad peaks,

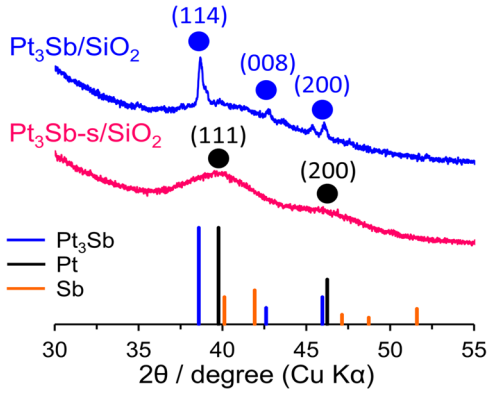

Figure 2. X-ray diffraction patterns of Pt_3Sb/SiO_2 and Pt_3Sb-s/SiO_2 catalysts. The vertical lines indicate the diffraction angles of the references: Pt,[34] Pt_3Sb,[35] and Sb.[35]

https://doi.org/10.1021/jacsau.5c00181
JACS Au 2025, 5, 1956−1964

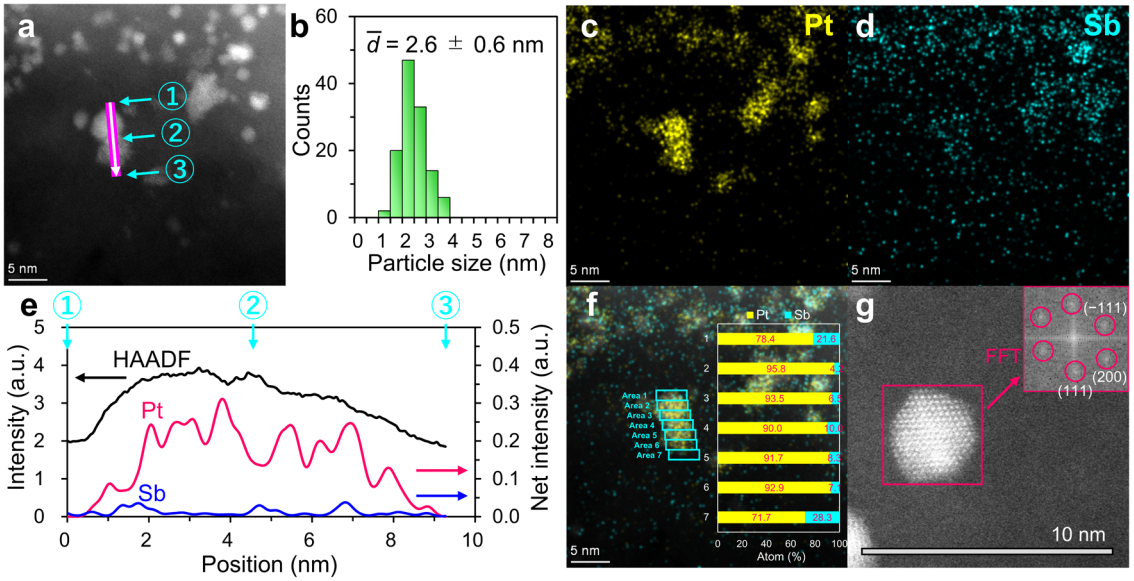

Figure 3. (a) HAADF-STEM image and (b) particle-size distribution of the Pt_3Sb-s/SiO_2 catalyst. Elemental maps of (c) Pt and (d) Sb of the Pt_3Sb-s/SiO_2 catalyst. (e) HAADF-STEM-EDX line-scan profiles of the Pt_3Sb-s/SiO_2 catalyst along the pink arrow shown in (a). (f) Quantitative analysis of the Pt_3Sb-s/SiO_2 catalyst. The atom% of Pt and Sb in the light blue squares is shown in the inset. (g) HAADF-STEM image of the Pt_3Sb-s/SiO_2 catalyst. The FFT shows that the crystalline phase of a nanoparticle is Pt.

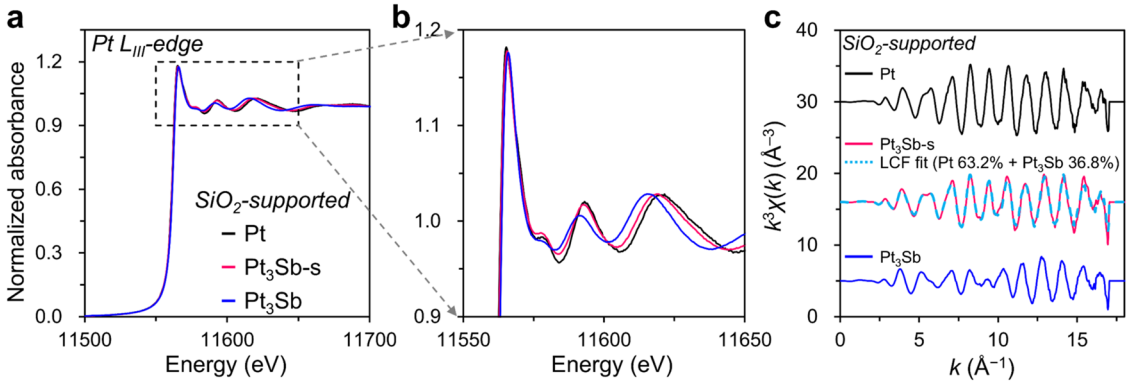

Figure 4. (a, b) Pt L_{III}-edge XANES spectra of Pt/SiO_2, Pt_3Sb-s/SiO_2, and Pt_3Sb/SiO_2. (b) Magnification of the region designated by dashed lines in (a). (c) Pt L_{III}-edge k^3-weighted extended X-ray absorption fine structure oscillations of the Pt/SiO_2, Pt_3Sb-s/SiO_2, and Pt_3Sb/SiO_2 catalysts. The linear combination fitting spectrum of the Pt_3Sb/SiO_2 catalyst using SiO_2-supported Pt and Pt_3Sb is indicated by a dashed line.

which match those of Pt, would be Pt−Pt_3Sb core−shell alloy nanoparticles. In contrast, the XRD patterns of the Pt_3Sb-s/SiO_2 catalyst agreed with those of monometallic Pt, and no detectable diffraction of Pt_3Sb was observed. Therefore, the bulk structures of the Pt_3Sb/SiO_2 and Pt_3Sb-s/SiO_2 catalysts are Pt_3Sb and monometallic Pt, respectively. The Pt dispersions estimated by the CO-pulse chemisorption are shown in Figure S6. As the amount of Sb was increased, the Pt dispersion decreased monotonically, implying that Pt was alloyed with Sb. However, for the Pt_3Sb/SiO_2 catalyst, the Pt dispersion level was close to zero. Therefore, Sb species can easily cover the surface of Pt_3Sb nanoparticles, probably because of the lower surface energy of Sb than that of Pt.[37] Thus, the Pt_3Sb/SiO_2 catalyst seems to be Pt_3Sb covered by excess Sb species (Figures S7 and S8). However, the structure of the Pt_3Sb-s/SiO_2 catalyst is still unclear. Therefore, we performed a structural analysis of the Pt_3Sb-s/SiO_2 catalyst. Particle-size distributions revealed that the mean particle size was 2.6 nm (Figure 3a,b). Energy-dispersive X-ray (EDX) analysis revealed that Pt and Sb coexisted in each nanoparticle (Figure 3c,d). However, the signals of Sb were also observed on SiO_2, indicating that some portions of the Sb species were located on the SiO_2 support and did not participate in alloying. The EDX line-scan profiles of the nanoparticles are shown in Figure 3e,f. Although the Pt signals were observed on the entire nanoparticle, the Sb signals were detected mainly at the edges of the nanoparticles. Furthermore, quantitative analysis of the nanoparticles revealed that the atomic ratios of Pt/Sb were close to 3 at the edge regions, whereas they were greater than 10 at the inner regions (Figure 3f). Notably, the quantitative results of the inner regions include the information on the edge parts. When the fast Fourier transform (FFT) was performed on the metal particle, diffraction spots derived from Pt were confirmed. These results suggested that the structure of the Pt_3Sb-s/SiO_2 catalyst would be the Pt−Pt_3Sb core−shell structure. However, the local structural information on the shell part is unclear.

Next, we performed X-ray absorption fine structure (XAFS) measurements. Figures 4a,b and S9 show the X-ray absorption near edge structure (XANES) spectra of the Pt L_{III}- and Sb K-

https://doi.org/10.1021/jacsau.5c00181
JACS Au 2025, 5, 1956−1964

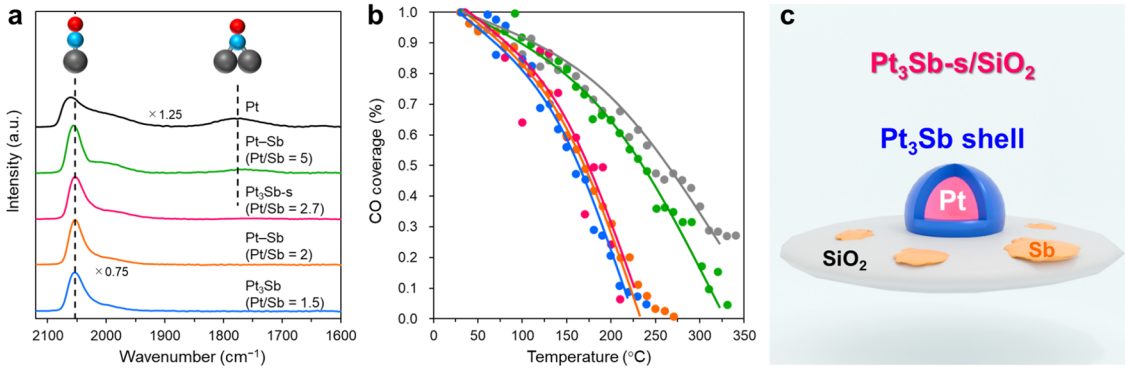

Figure 5. (a) FT-IR spectra of CO adsorbed on the Pt−Sb/SiO_2 catalysts at room temperature. (b) CO chemisorption surface coverage vs temperature for the Pt−Sb/SiO_2 catalysts. (c) Proposed structure of the Pt_3Sb-s/SiO_2 catalyst.

edges, respectively. Both Pt and Sb species were reduced to the metallic state, which was consistent with the H_2-TPR result. The XANES spectral features of the Pt_3Sb/SiO_2 and Pt_3Sb-s/SiO_2 catalysts were distinct from that of Pt/SiO_2, implying the formation of a Pt/Sb alloy upon the introduction of Sb. Figures 4c and S10 show the extended XAFS (EXAFS) and Fourier-transformed (FT) EXAFS spectra of the Pt L_{III}-edge, respectively. Notably, the atomic radius of Sb (1.39 Å) is slightly higher than that of Pt (1.36 Å).[27] Therefore, the Pt−Sb distance (R_{Pt-Sb}) becomes larger than the Pt−Pt distance (R_{Pt-Pt}) in random Pt−Sb solid-solution alloys. In contrast, the sparse crystal structure of the Pt_3Sb (Al_3Zr-type) makes the R_{Pt-Sb} shorter than the R_{Pt-Pt}, which is characteristic of this unique ordered crystal structure (FEFF calculation was performed in the crystallographic information file from ref 35). The EXAFS curve-fitting results for the Pt_3Sb/SiO_2 catalyst showed R_{Pt-Sb} and R_{Pt-Pt} of 2.65 and 2.75 Å, respectively (Table S1).[35,36] The peak intensity of Pt−Pt decreased, and a new peak assignable to Pt−Sb was observed at a relatively short distance (Figure S10). Combining the results of XRD, Pt dispersion, and XAFS, we concluded that the Pt_3Sb/SiO_2 catalyst is composed of nanoparticulate Pt_3Sb and the surface is covered by metallic Sb (a part of the Sb species is present on the SiO_2 support).

We also performed the EXAFS curve-fitting for the Pt_3Sb-s/SiO_2 catalyst (Figures 4, S10 and Table S1). When only Pt−Pt scattering was considered, curve-fitting provided reasonable data. By contrast, when Pt/Sb scattering was considered, the EXAFS Debye−Waller factor became negative (unreasonable). However, the raw-EXAFS spectrum showed a characteristic feature (*i.e.*, 5−10 $Å^{-1}$) that is not consistent with those of Pt/SiO_2 and solid-solution alloys (Figure 4c).[4] To further analyze the Pt_3Sb-s/SiO_2 catalyst structures, we performed linear combination fitting (Figure 4c). The raw-EXAFS spectral feature of Pt_3Sb-s/SiO_2 was well reproduced through the linear combination fitting of the Pt/SiO_2 (63.2%) and Pt_3Sb/SiO_2 (36.8%) catalysts, demonstrating that the shell portion in the Pt_3Sb-s/SiO_2 catalyst is a Pt_3Sb. Notably, the majority of metal−metal scattering is Pt−Pt scattering in the shell and core. Therefore, curve-fitting analysis, including a minority of Pt−Sb scattering, is highly arbitrary, and it could not provide substantial results (not the evidence of the absence of the Pt−Sb scattering). In addition, we performed linear combination fitting for Pt−Sb/SiO_2 with different Pt/Sb ratios (Figure S11). The lower the Pt/Sb ratio, the higher the percentage of the Pt_3Sb/SiO_2 component, indicating that the thickness of the Pt_3Sb shell can be tuned by changing the Pt/Sb ratio. When the Pt/Sb ratio is decreased to 1.5, the core part also becomes Pt_3Sb.

To comprehensively understand the surface structures, the surfaces of the Pt−Sb alloy nanoparticles were analyzed by *in situ* Fourier transform infrared (FT-IR) spectroscopy with CO adsorption (Figure 5a). For Pt/SiO_2, a peak, which was assigned to the linearly adsorbed CO on Pt, appeared at around 2065 cm^{-1}. In addition, a peak located at 1775 cm^{-1} was assigned to the bridged CO adsorbed on Pt. For Pt_3Sb/SiO_2, the bridged mode disappeared because of the dilution of the Pt ensembles by Sb to form a Pt_3Sb. Furthermore, Pt_3Sb-s/SiO_2 demonstrated an FT-IR spectrum that is almost similar to that of Pt_3Sb/SiO_2, which further indicates that the shell structure of Pt_3Sb/SiO_2 is a Pt_3Sb intermetallic. We also confirmed the FT-IR spectra of different Sb contents. In fact, when the Pt/Sb ratio was lower than 2.7 (Pt_3Sb-s/SiO_2), the Pt−Sb/SiO_2 catalyst showed Pt_3Sb/SiO_2-like spectra. By contrast, when the Pt/Sb ratio was >2.7 (Pt/Sb = 5), the bridged mode still remained, revealing that the Pt−Sb/SiO_2 catalyst (Pt/Sb = 5) was a mixture of Pt and Pt_3Sb surfaces. Figure 5b shows the CO chemisorption surface coverage versus the temperature monitored by FT-IR spectroscopy, which is sensitive to the formation of alloys on the surface.[38] The temperatures at which the coverage reaches 50% (T_{50}) are around 270 and 180 °C for Pt/SiO_2 and Pt_3Sb/SiO_2 (Pt/Sb = 1.5) catalysts, respectively. This result reveals that the changes in the structure of the surface alloy (in this case, from Pt to Pt_3Sb intermetallic) can be evident from the T_{50} values. Notably, the T_{50} values were close to 180 °C when the Pt/Sb ratio was lower than 2.7 (Pt_3Sb-s/SiO_2), which indicates that the shell portion of Pt_3Sb-s/SiO_2 is a Pt_3Sb intermetallic. In addition, no remarkable shift of the linearly bonded CO peak was observed with the increase in the Pt_3Sb shell thickness (Figure S11). Therefore, the electronic effect of Sb on Pt can be excluded from this study. Combining the results of XRD, Pt dispersion, HAADF-STEM-EDX, XAFS, and FT-IR spectroscopy, we concluded that the Pt_3Sb-s/SiO_2 catalyst is the Pt−Pt_3Sb core−shell nanoparticles, and some portion of Sb is located on SiO_2 in the metallic state (Figure 5c). Hence, we successfully synthesized the catalyst with distorted Pt_3 ensembles (Pt_3Sb-s/SiO_2), which can bridge theoretical prediction and experiment. By contrast, the Pt_3Sn/SiO_2[5,15] catalyst was synthesized in accordance with the literature with slight modifications (see Figure S12 for the XRD and XAFS results). The XRD patterns corresponded to those of referential Pt_3Sn (Cu_3Au-type). In addition, the EXAFS curve-fitting results showed R_{Pt-Pt} and R_{Pt-Sn} of 2.77 and

https://doi.org/10.1021/jacsau.5c00181
JACS Au 2025, 5, 1956−1964

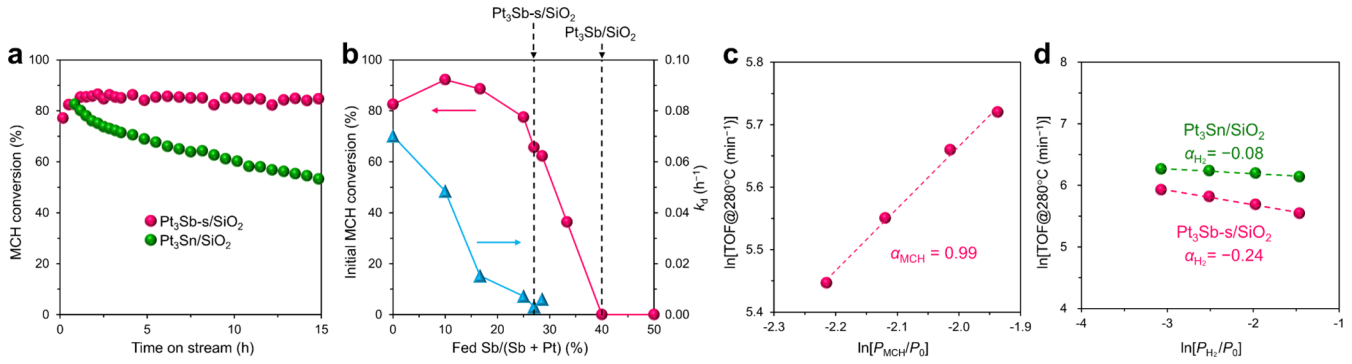

Figure 6. (a) MCH conversion of the Pt_3Sn/SiO_2 (10 mg) and Pt_3Sb-s/SiO_2 (20 mg) catalysts. Reaction conditions: 320 °C, MCH/He = 3.6/20, and F = 23.6 mL min^{-1}. (b) MCH conversion and catalyst stability (k_d) of the Pt−Sb/SiO_2 catalyst. Reduction condition: 700 °C for 1 h. Reaction conditions: 320 °C, MCH/He = 3.2/40, F = 43.2 mL min^{-1}, 20 mg of catalyst. (c) MCH partial dependence for MCH dehydrogenation on the Pt_3Sb-s/SiO_2 catalyst. Conditions: MCH/H_2/He = 3.6:x:y mL min^{-1}. x and y were adjusted not to change the PH_2/P_0 value of 0.15. Temperature was set at 280 °C. (d) Hydrogen partial dependence for MCH dehydrogenation on the Pt_3Sn/SiO_2 and Pt_3Sb-s/SiO_2 catalyst. Conditions: MCH/H_2/He = 3.2:x:40−x, F = 43.2 mL min^{-1}. Temperature was set at 280 °C.

2.78 Å, respectively (Table S1). These results reveal that the Pt_3Sb/SiO_2 catalyst has a Pt_3Sn intermetallic structure. In addition, we also used the $PtSn/SiO_2$ catalyst synthesized in the previous study.[4]

Effect of Platinum Distortion on the Catalytic Performance

Figure 6a compares the catalyst stability for MCH dehydrogenation over the Pt_3Sb-s/SiO_2 and Pt_3Sn/SiO_2 catalysts at 320 °C. When using the same catalyst, the apparent deactivation rates differ when varying the initial conversion levels probably because of the difference in H_2 concentration (Figure S13). Therefore, for a fair comparison of the deactivation behavior, the initial conversion levels shown in Figure 6a were adjusted to be close to 80%. During the 15 h, the Pt_3Sb-s/SiO_2 catalyst was not deactivated, whereas the Pt_3Sn/SiO_2 catalyst showed a rapid drop of conversion from 83 to 53%. To estimate the catalyst stability, the deactivation rate constant (k_d) was calculated using the first-order deactivation mode.[39] The lower the k_d, the higher the stability. k_d values of the Pt_3Sb-s/SiO_2 and Pt_3Sn/SiO_2 catalysts were 0.012 and 0.102h^{-1}, respectively. Therefore, the Pt_3Sb-s/SiO_2 catalyst is approximately 9 times more durable than the Pt_3Sn/SiO_2 catalyst. The control experiments were performed at different conversion levels for the Pt_3Sb-s/SiO_2 catalyst (Figures S14 and S15). Regardless of the conversion levels, almost no deactivation was observed, confirming outstanding durability.

Figure S16 shows the toluene selectivity at 400 °C under harsh conditions (MCH conversion: 100%). The selectivity of the Pt_3Sb-s/SiO_2 catalyst was 99.99%, which surpassed that of Pt/SiO_2 (99.90%) and Pt_3Sn/SiO_2 (99.97%). As mentioned, distorted and normal Pt_3 ensembles are present on the surfaces of the Pt_3Sb-s/SiO_2 and Pt_3Sn/SiO_2 catalysts, respectively. Therefore, these results demonstrate the excellent catalyst selectivity and durability of distorted Pt_3 ensembles compared with normal Pt_3 ensembles, as expected from the DFT calculations. Figure 6b shows the relationship between the Sb/(Sb + Pt) ratio and the catalytic activity or stability at 320 °C (refer to Figure S17 for the time on stream of MCH conversion). Upon the formation of the Pt−Pt_3Sb core−shell structure (Pt_3Sb-s/SiO_2), the catalyst stability was significantly improved, while the catalyst activity was slightly decreased due to the decrease in the Pt dispersion (Figure S6). Importantly, even when the Sb/(Sb + Pt) ratio was increased (increase in Pt_3Sb shell thickness), the catalyst acted stably. However, when Pt_3Sb formed on the core (Pt_3Sb/SiO_2), the catalyst showed no conversion because of the blockage of surface Pt sites by excess Sb (Figures S6 and S17). This result indicates the negligible contribution of Sb to the catalysis. It should be noted that for the stable catalyst where Pt_3Sb formed on the surface, a short induction period was observed at the initial stage of the reaction (Figure S17). As mentioned, inert Sb species tend to be deposited on the surface of the nanoparticles. Therefore, a possible interpretation is the redistribution of excess Sb from a part of the surface Pt sites to the SiO_2 support. A similar phenomenon has been reported for the Pb-decorated PtGa system.[5,7]

To confirm the effect of ensemble size on the catalytic activity, a control experiment was performed using the PtSn/SiO_2 catalyst (Figure S17). Generally, one-dimensionally aligned Pt columns separated by Sn function as active sites (the surface Pt−Pt coordination number is only two) in the PtSn intermetallic.[20] The $PtSn/SiO_2$ catalyst showed a comparably low catalytic activity, supporting the fact that Pt ensembles larger than two act as active sites for this reaction and the Pt_3Sb-s/SiO_2 and Pt_3Sn catalysts have Pt_3 ensembles. As stated, all Pt_3 ensembles on the Pt_3Sb nanoparticle are distorted because of the crystallographically unique crystal structure (Figure S2). Thus, we concluded that the outstanding durability of the Pt_3Sb-s/SiO_2 catalyst originated from the distorted Pt_3 ensembles.

Additionally, a kinetic study of the Pt_3Sb-s/SiO_2 catalyst was performed. The reaction order (α_{MCH}) of MCH partial pressure was close to 1, indicating that one of the C−H scissions to form toluene from MCH is a rate-determining step (Figure 6c) as reported in the literature.[26,40] Further, the reaction order of hydrogen pressure (α_{H_2}) was estimated (Figure 6d). Interestingly, α_{H_2} showed a negative value of −0.24, suggesting moderate hydrogen poisoning. For the conventional Pt_3M (M = Fe, Sn, In), the values of α_{H_2} were close to zero.[15] Additionally, we confirmed that the α_{H_2} value for the Pt_3Sn/SiO_2 catalyst was close to zero (Figure 6d), implying a characteristic nature of Pt_3Sb. Regarding propane dehydrogenation, it has been reported that alloying Pt with metalloid Ge triggers hydrogen poisoning,[41] suggesting that the hydrogen poisoning was induced by the incorporation of the metalloid Sb. The energy barriers for hydrogen association

https://doi.org/10.1021/jacsau.5c00181
JACS Au 2025, 5, 1956−1964

were calculated (Figure S18). $Pt_3Sb(114)$ showed a higher value of 94.3 kJ mol^{-1} than $Pt_3Sn(111)$ (82.2 kJ mol^{-1}). Therefore, the sluggish desorption of hydrogen from the surface decreased the number of adsorption sites for MCH, thereby attenuating the catalytic activity of the Pt_3Sb-s/SiO_2 catalyst. To confirm the role of coadsorbed hydrogen in catalyst durability, we calculated the ΔE value for Pt_3@$Pt_3Sb(114)$ with coadsorbed hydrogen species (Figure S19), which showed a similar value of 197.5 kJ mol^{-1} to that without coadsorbed hydrogen (Figure S4). Therefore, the presence of coadsorbed hydrogen does not significantly change the catalyst durability. Notably, the Pt_3Sb-s/SiO_2 catalyst exhibited high catalyst durability at various conversion levels (different H_2 concentrations), highlighting the intrinsically high catalyst durability of the distorted Pt_3 ensembles for MCH dehydrogenation (Figures S14 and S15).

Again, the DFT calculations suggested that the difference in adsorption configurations is the key to improving durability. Therefore, we performed temperature-programmed toluene desorption with an adsorption temperature of 50 °C (Figure S20). Unfortunately, SiO_2 itself showed a large desorption peak. Although the presence of alloy nanoparticles resulted in the promoted desorption of toluene, the large contribution of SiO_2 itself drowned out the difference between Pt_3Sb-s/SiO_2 and Pt_3Sn/SiO_2. Finally, a long-term stability test was performed using the Pt_3Sb-s/SiO_2 catalyst at 300 °C (Figure S21). The Pt_3Sb-s/SiO_2 catalyst exhibited an initial conversion of 83% and underwent gradual deactivation, resulting in a 51% conversion after 200 h. XAFS measurement and FT-IR spectroscopy with CO adsorption revealed no remarkable dynamic change in the structures of whole nanoparticles and Pt_3Sb-type surfaces before and after the reaction (Figure S22). Therefore, the distorted Pt_3@Pt_3Sb shell in the Pt_3Sb-s/SiO_2 catalyst can serve as an active site under the reaction conditions. However, a slight decrease in the Pt dispersion was observed (Figure S6). Large nanoparticles were observed for the spent catalyst, in addition to small nanoparticles (Figure S23). Therefore, the aggregation of nanoparticles may contribute to the deactivation of the Pt_3Sb-s/SiO_2 catalyst during the MCH reaction rather than the collapse of the core–shell structures. It should be noted that excess Sb species were present on the SiO_2 support in the metallic state, which might trigger the sintering of nanoparticles. Therefore, if the excess Sb can be strongly anchored on the support in the oxidation state, the catalyst would be more stable even in the long-term catalytic operation.

CONCLUSIONS

Here, we demonstrate the importance of the ensemble shape. Two different shapes of the Pt_3 ensembles were provided by the Cu_3Au-type Pt_3Sn and $ZrAl_3$-type Pt_3Sb, respectively. The former was an equirectangular triangle, whereas the latter was an isosceles triangle. These alloy materials have similar electronic structures, and the atomic radii are almost the same. Therefore, only the Pt_3 ensemble shapes were significantly different among these alloy materials. Interestingly, Pt_3Sb exhibited considerably higher durability than Pt_3Sn for the test reaction of MCH. Theoretical and experimental results showed that the distorted Pt_3 ensembles of Pt_3Sb effectively suppressed the side reactions and exhibited considerably higher catalyst durability than the normal Pt_3 ensembles of Pt_3Sn. This study showed the impact of the ensemble shape and demonstrated the decoupling of the geometric effect of alloy catalysis from the entanglement geometric–electronic relationship for the first time. This work provides an effective strategy for exploring the fundamental insights of alloy catalysis, and thus it helps to design catalysts with unprecedented properties.

METHODS

Materials

$Pt(NH_3)_2(NO_3)_2$ (Tanaka Precious Metals Co. Ltd., 4.60 wt % Pt in HNO_3 solution), SbF_3 (Wako, 98%), $(NH_4)_2SnCl_6$ (Alfa Aesar, 98%), SiO_2 (CARiACT G-6, Fuji Silysia, $S_{BET} \approx 500$ m^2 g^{-1}), and methylcyclohexane (MCH; Wako, ≥98%) were used in this study.

Catalyst Preparation

The as-prepared Pt_3Sb-s/SiO_2 catalyst was synthesized through pore-filling co-impregnation.[5,6,17,33] The Pt/Sb molar ratio was fixed at 2.7 (Sb: 0.69 wt %). A mixed aqueous solution of $Pt(NH_3)_2(NO_3)_2$, SbF_3, and ion-exchanged water was added dropwise to SiO_2 (1.6 mL of the solution per gram of SiO_2). The obtained mixture was sealed to prevent water evaporation and kept overnight at room temperature. Thereafter, the mixture was transferred to a round-bottom flask, frozen using liquid nitrogen, and dried in a vacuum at approximately −5 °C. The dried sample was further dried in an oven at 90 °C overnight and then calcined at 400 °C for 1 h in dry air with a ramping rate of 1 °C min^{-1}. The as-prepared Pt_3Sb/SiO_2 catalyst was synthesized following a procedure similar to that of the as-prepared Pt_3Sb-s/SiO_2 catalyst; however, the Pt/Sb ratio was 1.5 (Sb: 1.25 wt %). The as-prepared Pt_3Sn/SiO_2 catalyst was synthesized following a procedure similar to that of the as-prepared Pt_3Sb-s/SiO_2 catalyst. The Pt/Sn molar ratio was fixed at 3, and $(NH_4)_2SnCl_6$ was used as the precursor instead of SbF_3. The as-prepared $PtSn/SiO_2$ catalyst was synthesized following a procedure similar to that of the as-prepared Pt_3Sn/SiO_2 catalyst. The Pt/Sn molar ratio was fixed at 1.

ASSOCIATED CONTENT

Supporting Information

The Supporting Information is available free of charge at https://pubs.acs.org/doi/10.1021/jacsau.5c00181.

Details for DFT calculations; routine characterization; and catalytic tests (PDF)

AUTHOR INFORMATION

Corresponding Authors

Yuki Nakaya − *Division of Applied Chemistry, Graduate School of Engineering, Osaka University, Suita 565-0871 Osaka, Japan;* orcid.org/0000-0001-8457-1369; Email: nakaya@chem.eng.osaka-u.ac.jp

Shinya Furukawa − *Division of Applied Chemistry, Graduate School of Engineering, Osaka University, Suita 565-0871 Osaka, Japan;* orcid.org/0000-0002-2621-6139; Email: furukawa@chem.eng.osaka-u.ac.jp

Author

Aoto Okada − *Division of Applied Chemistry, Graduate School of Engineering, Osaka University, Suita 565-0871 Osaka, Japan;* orcid.org/0009-0000-2788-8538

Complete contact information is available at: https://pubs.acs.org/10.1021/jacsau.5c00181

Author Contributions

Y.N. and S.F. supervised the study. Y.N. and A.O. performed the experiments. Y.N. carried out the theoretical calculations. Y.N. and S.F. discussed and revised the paper.

Funding

This work was supported by JSPS KAKENHI (Grant Numbers 20H02517, 21J20594, 22KJ0016, 22K18336, 23H00308, and 24K23105). Travel expenses and user fees for this synchrotron radiation experiment were supported by the JASRI Research Student by JASRI through the Long-term Graduate Student Proposal (Nos. 2023A0302 and 2023B0302).

Notes

The authors declare no competing financial interest.

■ ACKNOWLEDGMENTS

The XAFS measurement was performed at the BL01B1 beamline of SPring-8 at the JASRI (Nos. 2023A0302 2023B0302, and 2024B2022). HAADF-STEM observation was supported by Advanced Research Infrastructure for Materials and Nanotechnology in Japan (ARIM, Proposal Nos: JPMXP1222HK0056, JPMXP1223HK0026, and JPMXP1224HK0055) and the Joint Usage/Research Center for Catalysis (Proposal No. 24AY0700). Computation time was provided by the supercomputer systems in the Institute for Chemical Research at Kyoto University.

■ REFERENCES

(1) Nakaya, Y.; Furukawa, S. Catalysis of Alloys: Classification, Principles, and Design for a Variety of Materials and Reactions. *Chem. Rev.* **2023**, *123*, 5859−5947.
(2) Furukawa, S.; Komatsu, T.; Shimizu, K. I. Catalyst Design Concept Based on a Variety of Alloy Materials: A Personal Account and Relevant Studies. *J. Mater. Chem. A* **2020**, *8*, 15620−15645.
(3) Yu, W.; Porosoff, M. D.; Chen, J. G. Review of Pt-Based Bimetallic Catalysis: From Model Surfaces to Supported Catalysts. *Chem. Rev.* **2012**, *112*, 5780−5817.
(4) Nakaya, Y.; Hayashida, E.; Asakura, H.; Takakusagi, S.; Yasumura, S.; Shimizu, K.; Furukawa, S. High-Entropy Intermetallics Serve Ultrastable Single-Atom Pt for Propane Dehydrogenation. *J. Am. Chem. Soc.* **2022**, *144*, 15944−15953.
(5) Nakaya, Y.; Hirayama, J.; Yamazoe, S.; Shimizu, K.; Furukawa, S. Single-Atom Pt in Intermetallics as an Ultrastable and Selective Catalyst for Propane Dehydrogenation. *Nat. Commun.* **2020**, *11*, No. 2838.
(6) Stephens, I. E. L.; Bondarenko, A. S.; Perez-Alonso, F. J.; Calle-Vallejo, F.; Bech, L.; Johansson, T. P.; Jepsen, A. K.; Frydendal, R.; Knudsen, B. P.; Rossmeisl, J.; Chorkendorff, I. Tuning the Activity of Pt(111) for Oxygen Electroreduction by Subsurface Alloying. *J. Am. Chem. Soc.* **2011**, *133*, 5485−5491.
(7) Nakaya, Y.; Xing, F.; Ham, H.; Shimizu, K.; Furukawa, S. Doubly Decorated Platinum−Gallium Intermetallics as Stable Catalysts for Propane Dehydrogenation. *Angew. Chem., Int. Ed.* **2021**, *60*, 19715−19719.
(8) Chen, S.; Zhao, Z.; Mu, R.; Chang, X.; Luo, J.; Purdy, S. C.; Kropf, A. J.; Sun, G.; Pei, C.; Miller, J. T.; Zhou, X.; Vovk, E.; Yang, Y.; Gong, J. Propane Dehydrogenation on Single-Site [$PtZn_4$] Intermetallic Catalysts. *Chem* **2021**, *7*, 387−405.
(9) Sun, G.; Zhao, Z. J.; Mu, R.; Zha, S.; Li, L.; Chen, S.; Zang, K.; Luo, J.; Li, Z.; Purdy, S. C.; Kropf, A. J.; Miller, J. T.; Zeng, L.; Gong, J. Breaking the Scaling Relationship via Thermally Stable Pt/Cu Single Atom Alloys for Catalytic Dehydrogenation. *Nat. Commun.* **2018**, *9*, No. 4454.
(10) Sun, S.; Sun, G.; Pei, C.; Zhao, Z. J.; Gong, J. Origin of Performances of Pt/Cu Single-Atom Alloy Catalysts for Propane Dehydrogenation. *J. Phys. Chem. C* **2021**, *125*, 18708−18716.
(11) Miyazaki, M.; Furukawa, S.; Komatsu, T. Correlation between Activation Energy and the Electronic State of Pd-Based Bimetallic Catalysts for H_2-D_2 Equilibration Obtained by XPS and DFT Calculations. *Bull. Chem. Soc. Jpn.* **2020**, *93*, 1020−1025.
(12) Chang, X.; Lu, Z.; Wang, X.; Zhao, Z. J.; Gong, J. Tracking C-H Bond Activation for Propane Dehydrogenation over Transition Metal Catalysts: Work Function Shines. *Chem. Sci.* **2023**, *14*, 6414−6419.
(13) Stamenkovic, V.; Mun, B. S.; Mayrhofer, K. J. J.; Ross, P. N.; Markovic, N. M.; Rossmeisl, J.; Greeley, J.; Nørskov, J. K. Changing the Activity of Electrocatalysts for Oxygen Reduction by Tuning the Surface Electronic Structure. *Angew. Chem., Int. Ed.* **2006**, *45*, 2897−2901.
(14) Escudero-Escribano, M.; Malacrida, P.; Hansen, M. H.; Vej-Hansen, U. G.; Velázquez-Palenzuela, A.; Tripkovic, V.; Schiøtz, J.; Rossmeisl, J.; Stephens, I. E. L.; Chorkendorff, I. Tuning the Activity of Pt Alloy Electrocatalysts by Means of the Lanthanide Contraction. *Science* **2016**, *352*, 73−76.
(15) Nakaya, Y.; Miyazaki, M.; Yamazoe, S.; Shimizu, K.; Furukawa, S. Active, Selective, and Durable Catalyst for Alkane Dehydrogenation Based on a Well-Designed Trimetallic Alloy. *ACS Catal.* **2020**, *10*, 5163−5172.
(16) Chen, L.; Verma, P.; Hou, K.; Qi, Z.; Zhang, S.; Liu, Y. S.; Guo, J.; Stavila, V.; Allendorf, M. D.; Zheng, L.; Salmeron, M.; Prendergast, D.; Somorjai, G. A.; Su, J. Reversible Dehydrogenation and Rehydrogenation of Cyclohexane and Methylcyclohexane by Single-Site Platinum Catalyst. *Nat. Commun.* **2022**, *13*, No. 1092.
(17) Furukawa, S.; Matsunami, Y.; Hamada, I.; Hashimoto, Y.; Sato, Y.; Komatsu, T. Remarkable Enhancement in Hydrogenation Ability by Phosphidation of Ruthenium: Specific Surface Structure Having Unique Ru Ensembles. *ACS Catal.* **2018**, *8*, 8177−8181.
(18) Ye, T. N.; Lu, Y.; Xiao, Z.; Li, J.; Nakao, T.; Abe, H.; Niwa, Y.; Kitano, M.; Tada, T.; Hosono, H. Palladium-Bearing Intermetallic Electride as an Efficient and Stable Catalyst for Suzuki Cross-Coupling Reactions. *Nat. Commun.* **2019**, *10*, No. 5653.
(19) Ma, J.; Xing, F.; Nakaya, Y.; Shimizu, K.; Furukawa, S. Nickel-Based High-Entropy Intermetallic as a Highly Active and Selective Catalyst for Acetylene Semihydrogenation. *Angew. Chem., Int. Ed.* **2022**, *61* (27), No. e202200889.
(20) Xing, F.; Ma, J.; Shimizu, K.; Furukawa, S. High-Entropy Intermetallics on Ceria as Efficient Catalysts for the Oxidative Dehydrogenation of Propane Using CO_2. *Nat. Commun.* **2022**, *13*, No. 5065.
(21) Momma, K.; Izumi, F. VESTA 3 for Three-Dimensional Visualization of Crystal, Volumetric and Morphology Data. *J. Appl. Crystallogr.* **2011**, *44*, 1272−1276.
(22) Segall, M. D.; Lindan, P. J. D.; Probert, M. J.; Pickard, C. J.; Hasnip, P. J.; Clark, S. J.; Payne, M. C. First-Principles Simulation: Ideas, Illustrations and the CASTEP Code. *J. Phys.: Condens. Matter* **2002**, *14*, 2717−2744.
(23) Biniwale, R. B.; Rayalu, S.; Devotta, S.; Ichikawa, M. Chemical Hydrides: A Solution to High Capacity Hydrogen Storage and Supply. *Int. J. Hydrogen Energy* **2008**, *33*, 360−365.
(24) James, O. O.; Mandal, S.; Alele, N.; Chowdhury, B.; Maity, S. Lower Alkanes Dehydrogenation: Strategies and Reaction Routes to Corresponding Alkenes. *Fuel Process. Technol.* **2016**, *149*, 239−255.
(25) Sekine, Y.; Higo, T. Recent Trends on the Dehydrogenation Catalysis of Liquid Organic Hydrogen Carrier (LOHC): A Review. *Top. Catal.* **2021**, *64*, 470−480.
(26) Alhumaidan, F.; Cresswell, D.; Garforth, A. Hydrogen Storage in Liquid Organic Hydride: Producing Hydrogen Catalytically from Methylcyclohexane. *Energy Fuels* **2011**, *25*, 4217−4234.
(27) Cordero, B.; Gómez, V.; Platero-Prats, A. E.; Revés, M.; Echeverría, J.; Cremades, E.; Barragán, F.; Alvarez, S. Covalent Radii Revisited. *J. Chem. Soc. Dalton Trans.* **2008**, *21*, 2832−2838.
(28) Nykänen, L.; Honkala, K. Density Functional Theory Study on Propane and Propene Adsorption on Pt(111) and PtSn Alloy Surfaces. *J. Phys. Chem. C* **2011**, *115*, 9578−9586.
(29) Yang, M. L.; Zhu, Y. A.; Zhou, X. G.; Sui, Z. J.; Chen, D. First-Principles Calculations of Propane Dehydrogenation over PtSn Catalysts. *ACS Catal.* **2012**, *2*, 1247−1258.
(30) Nykänen, L.; Honkala, K. Selectivity in Propene Dehydrogenation on Pt and Pt_3Sn Surfaces from First Principles. *ACS Catal.* **2013**, *3*, 3026−3030.

https://doi.org/10.1021/jacsau.5c00181
JACS Au 2025, 5, 1956−1964

(31) Zha, S.; Sun, G.; Wu, T.; Zhao, J.; Zhao, Z. J.; Gong, J. Identification of Pt-Based Catalysts for Propane Dehydrogenation: Via a Probability Analysis. *Chem. Sci.* **2018**, *9*, 3925−3931.
(32) Nakaya, Y.; Furukawa, S. Tailoring Single-Atom Platinum for Selective and Stable Catalysts in Propane Dehydrogenation. *ChemPlusChem* **2022**, *87*, No. e202100560.
(33) Manabe, S.; Yabe, T.; Nakano, A.; Nagatake, S.; Higo, T.; Ogo, S.; Nakai, H.; Sekine, Y. Theoretical Investigation on Structural Effects of Pt−Mn Catalyst on Activity and Selectivity for Methylcyclohexane Dehydrogenation. *Chem. Phys. Lett.* **2018**, *711*, 73−76.
(34) Tripathi, S. N.; Chandrasekharaiah, M. S. Thermodynamic Properties of Binary Alloys of Platinum Metals II: Ir-Pt System. *J. Less-Common Met.* **1983**, *91*, 251−260.
(35) Kim, W.-S. Solid State Phase Equilibria in the Pt−Sb−Te System. *J. Alloys Compd.* **1997**, *252*, 166−171.
(36) Kojima, T.; Nakaya, Y.; Ham, H.; Kameoka, S.; Furukawa, S. Synthesis of Co_2FeGe Heusler Alloy Nanoparticles and Catalysis for Selective Hydrogenation of Propyne. *RSC Adv.* **2021**, *11*, 18074−18079.
(37) Vitos, L.; Ruban, A. V.; Skriver, H. L.; Kollár, J. The Surface Energy of Metals. *Surf. Sci.* **1998**, *411*, 186−202.
(38) Wu, Z.; Bukowski, B. C.; Li, Z.; Milligan, C.; Zhou, L.; Ma, T.; Wu, Y.; Ren, Y.; Ribeiro, F. H.; Delgass, W. N.; Greeley, J.; Zhang, G.; Miller, J. T. Changes in Catalytic and Adsorptive Properties of 2 Nm Pt_3Mn Nanoparticles by Subsurface Atoms. *J. Am. Chem. Soc.* **2018**, *140*, 14870−14877.
(39) Sattler, J. J. H. B.; Ruiz-Martinez, J.; Santillan-Jimenez, E.; Weckhuysen, B. M. Catalytic Dehydrogenation of Light Alkanes on Metals and Metal Oxides. *Chem. Rev.* **2014**, *114*, 10613−10653.
(40) Oshima, K.; Ito, H.; Yamamoto, T.; Kishida, M. Kinetics Analysis of Methylcyclohexane Dehydrogenation over Se-Modified Pt/TiO_2 Catalysts. *J. Chem. Eng. Jpn.* **2024**, *57*, No. 2301533.
(41) Rimaz, S.; Kosari, M.; Chen, L.; Xi, S.; Monzon, A.; Kawi, S.; Borgna, A. Insights into Catalyst Structure, Kinetics and Reaction Mechanism during Propane Dehydrogenation on Pt-Ge Bimetallic Catalysts. *Appl. Catal., A* **2022**, *643*, No. 118751.

https://doi.org/10.1021/jacsau.5c00181
JACS Au 2025, 5, 1956−1964